Soluble-Salt-Induced Embedding of Metal Catalysts into Gas Diffusion Electrodes for Electrochemical CO$_2$ Reduction to Formate

Chuanhao Wang, Yizhou Dai, Xian Zhong, Wenrui Zhang, Zhaoyang Chen, Chunxiao Liu, Yuan Ji, Sunpei Hu, Alexander Kostis, Adrian Schlüter, Eko Budiyanto, Boyan Zhang, Chih-Wen Pao, Yizhen Chen, Florian Baum, Jacob Johny, Xu Li, Qiu Jiang, Hong-Jie Peng, Xinyan Liu, Jie Zeng, Tingting Zheng,* and Chuan Xia

ACCESS | Metrics & More | Article Recommendations | Supporting Information

ABSTRACT: Electrochemical CO$_2$ reduction to formic acid (HCOOH) has great potential for reducing the carbon footprint and producing liquid fuel. Although several *p*-block metals have been recognized to be formate-selective, the flooding of catholytes into the catalyst layer at high current densities significantly promotes the competing hydrogen evolution reaction (HER), compromising the efficiency. Here, we report a soluble-salt-inducing fabrication method to disperse formate-selective metals into the carbon matrix of gas diffusion electrodes, in contrast to the conventional surface-supported architectures. This deep metal infiltration effectively suppresses HER under flooding conditions, enabling high formate Faradaic efficiencies of 93% across a broad current density ranging from −50 to −900 mA cm^{-2}, using chloride-derived indium (CD-In) as a model catalyst. An unexpected compressive strain of 2−4% is also identified as the origin of the faster kinetics over CD-In. Furthermore, we demonstrate the generality of this method with other formate-selective metals, highlighting its potential for scalable CO$_2$ electroreduction.
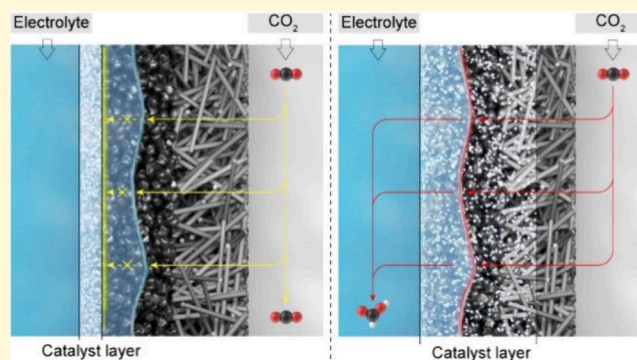
E lectrochemical CO$_2$ reduction reaction (CO$_2$RR) into value-added chemicals and fuels is central to closing the anthropogenic carbon cycle and enabling carbon-neutral energy systems.[1,2] Formic acid (HCOOH), a portable fuel with high energy density and low toxicity, exhibits the highest profit per electron among various CO$_2$RR products,[3] including CO,[4] ethylene,[5−7] ethanol,[8,9] and *n*-propanol.[10] In particular, p-block metals such as indium (In), bismuth (Bi), and tin (Sn)-based catalysts have demonstrated high selectivity for HCOOH or formate.[11−15] Based on the selectivity over different metal electrodes reported by Hori,[16] Bagger et al. classified metals with CO* and H* adsorption energy obtained from density functional theory (DFT) calculations and established that selectivity is strongly correlated with H* binding strength.[17] For formate-selective metals, which are characteristic of high H* binding energy, suppression of competing HER should, in principle, be feasible and operable.[17]

In gas diffusion electrode (GDE)-based flow cells, where gaseous CO$_2$ is supplied directly to the catalyst-electrolyte interface,[18] it is feasible to achieve high current density (≥500 mA cm^{-2}), though HER could become dominant, significantly reducing the Faradaic efficiency (FE) toward formate and diminishing the economic viability of the process. This

discrepancy should not arise from the intrinsic catalytic limitations, which has already been demonstrated from the theoretic analysis,[17] but from interfacial change and mass transport. At triple-phase boundaries (TPBs), alkali metal cations (AMCs) also get involved in CO$_2$RR to stabilize multiple intermediates via cation-coupled electron transfer mechanism.[19,20] Despite their dispensability, AMCs exhibit a side effect by the formation of (bi)carbonate precipitation, which further serves as the hydrophilic center to induce aqueous solution penetration into the GDE, known as flooding issue. This inevitable flooding issue is more pronounced at high current density, where water consumption is faster and the AMCs are more enriched.[21] *Operando* neutron imaging has revealed that flooded condition significantly lowers CO$_2$ availability and thus creates a HER-favorable microenvironment even on nominally selective catalysts.[22]
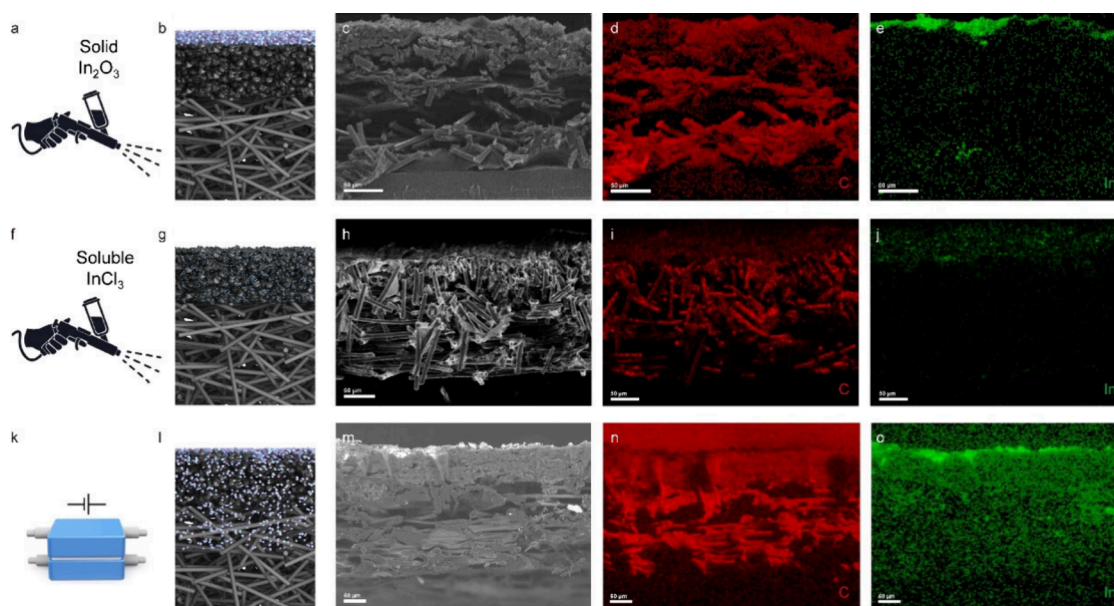
Figure 1. Differences in the spatial distribution of In in GDEs fabricated by conventional solid-involved coating and soluble-salt inducing method. **a**) Schematic diagram of the conventional solid-involved coating method. **b**) Schematic diagram of the spatial distribution of catalysts in GDEs fabricated by the conventional solid-involved coating method. **c**) Cross-sectional SEM image of an OD-In-loaded GDE. **d**) C and **e**) In elemental EDX mapping of the OD-In loaded GDE. **f**) Schematic diagram of the soluble-salt-inducing method. **g**) Schematic diagram of the spatial distribution of the precursor in the GDE fabricated by the soluble-salt-inducing method. **h**) Cross-sectional SEM image of an InCl₃-loaded GDE. **i**) C and **j**) In elemental EDX mapping of the InCl₃-loaded GDE. **k**) Schematic diagram of electroreduction of the salt precursor. **l**) Schematic diagram of the spatial distribution of the catalyst in GDE fabricated by the soluble-salt-inducing method. **m**) Cross-sectional SEM image of a CD-In-loaded GDE. **n**) C and **o**) In elemental EDX mapping of the CD-In-loaded GDE. Scale bar, 50 μm. $NaHCO_3$ and $NaOH$ were used as the catholyte and anolyte to prevent the overlap between In and K.

Conventional strategies to boost formate-selective production have primarily focused on catalyst-level modifications such as alloying, defect engineering, and phase control, aiming at optimizing adsorption energetics and accelerating CO_2RR.[11,13−15] These efforts seek to overcome the potential intrinsic activity limits of formate-selective metals and avoid the onset of the HER as the dominant pathway. However, such approaches often overlook the critical role of catalyst-electrolyte interface regulation, which remains difficult to probe with current *operando* techniques. As a result, the suppression of HER, particularly under high current densities or prolonged operation, where electrode flooding becomes severe, remains an unsolved challenge. A universal strategy that addresses these interfacial limitations is still lacking, continuing to obscure the realization of the intrinsic catalyst selectivity predicted by theory.

Herein, inspired by the zeolite-encapsulated particles widely used in thermocatalysis,[23−25] we propose a universal soluble-salt-inducing strategy to disperse formate-selective metals into the carbon matrix of GDE. Using In as a model system, the resulting catalyst domain formed a vertically distributed architecture with a penetration depth of ∼ 150 μm, where small CD-In particles were dispersed throughout the carbon black layer and immigrated into the carbon fiber layer. By contrast, spray-coated oxide-derived indium (OD-In), representative of conventionally fabricated GDEs, was confined to the top of the carbon black layer with a depth of <30 μm. The embedded architecture slowed down the loss of TPBs. As a result, CD-In delivered formate FE > 93% with HER FE < 2% across a wide current-density range from −50 to −900 mA cm⁻², whereas HER increased markedly with current density for OD-In. Additionally, a compressive strain of 2 ∼ 4% was

observed on the smaller CD-In particles, which may account for the faster kinetics evidenced by *in situ* Raman results and Tafel slopes. The generality of this fabrication strategy was further demonstrated by extending it to soluble Bi and Sn precursors.

To address the imbalance of the gas-electrolyte interface at a high current density, we started with a structural analysis of a commercial carbon paper GDL (YLS-30). This commercial GDL consisted of a carbon fiber layer with a thickness of ∼ 150 μm for gas transportation and a carbon black layer with a thickness of ∼ 50 μm for catalyst support, evidenced by a cross-sectional scanning electron microscopy (SEM) image (Figure S1). As a benchmark, OD-In was prepared by spraying a coating of In_2O_3 onto the GDL followed by *in situ* electroreduction (Figures 1a and S2). The cross-sectional SEM image of the OD-In loaded GDE and its corresponding energy-dispersive X-ray (EDX) elemental mapping indicated that In was supported on the upper surface of GDL (Figure 1b-e), consistent with previous reports using a conventional solid-coating strategy including spray coating and physical vapor deposition.[26−28]

To optimize catalyst distribution and minimize flooding-induced performance degeneration, we developed a soluble-salt-inducing synthesis method. Soluble $InCl_3$ was first dissolved into isopropanol (IPA), chosen for its wetting affinity to carbon, and then the solution was air-brushed onto the GDL (Figures 1f-i, S2, and S3a). SEM-EDX mapping showed that the In precursor distributed uniformly in the carbon black layer, strongly different from the surface-supported behavior observed on OD-In (Figure 1a-e). No detectable hydrolysis to (hydr)oxide or decomposition to metallic indium was observed, as confirmed by the X-ray
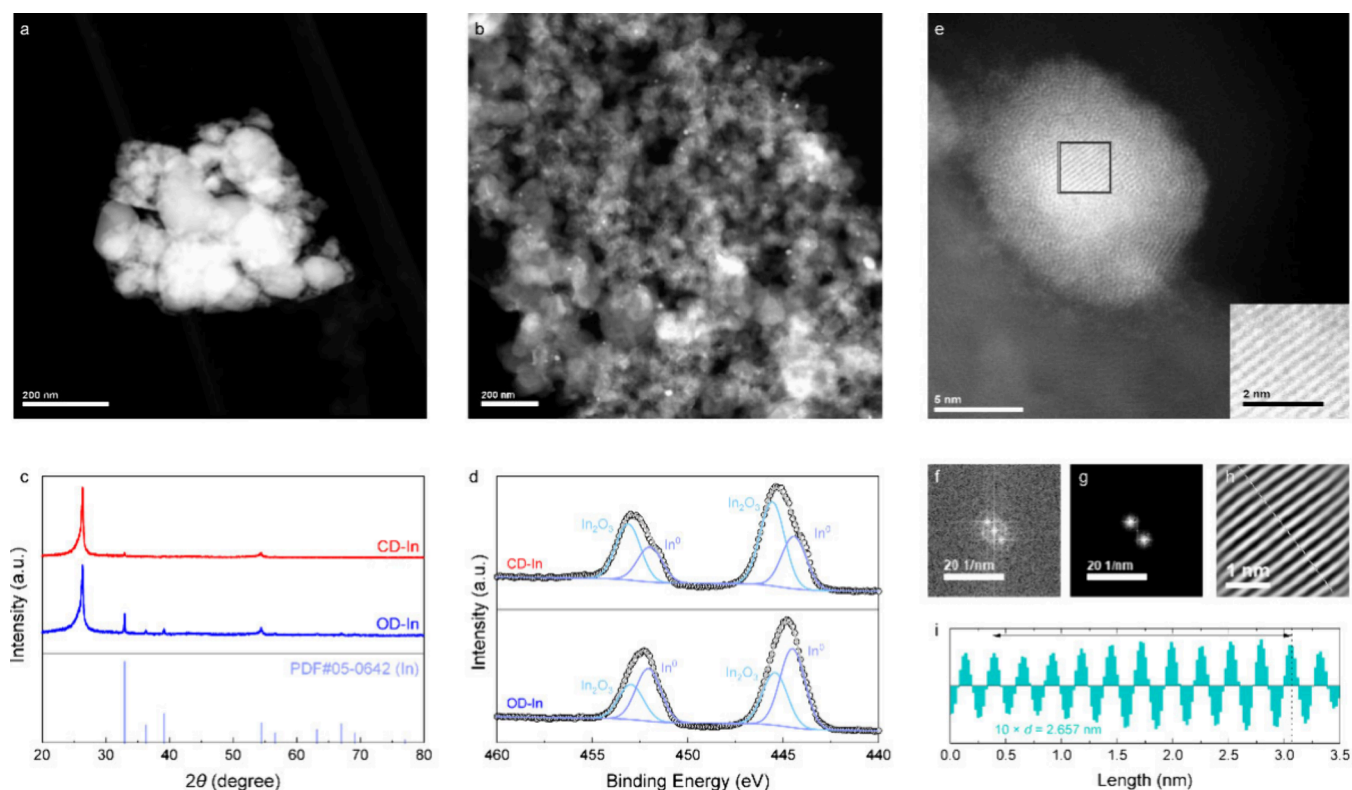
Figure 2. Structural characterization of CD-In and OD-In. **a**) HAADF-STEM image of OD-In. Scale bar: 200 nm. **b**) HAADF-STEM image of CD-In. Scale bar, 200 nm. **c**) XRD patterns of a CD-In-loaded GDE and an OD-In-loaded GDE. **d**) XPS spectra of CD-In loaded GDE and OD-In loaded GDE. **e**) Atomic-resolution HAADF-STEM image of selected particles in CD-In. Scale bar, 5 nm. The inset is the area in the white box. Scale bar, 2 nm. **f**) FFT of the inset area of **e**). **g**) The masked result of **f**). **h**) IFFT of **g**). **i**) Profile along the white line in **h**).

diffraction (XRD) pattern (Figure S2). Since the ionic $InCl_3$ was confined in the carbon black layer, the GDL surface retained partial hydrophobicity with the presence of a water droplet (Figure S4). When the $KHCO_3$ solution was flowed into the cathodic chamber, $InCl_3$ on the surface was immediately hydrolyzed, and hydrolyzed species with loose binding was easily flushed away after the electroreduction process to fabricate CD-In (Figure S5). $NaHCO_3$ and NaOH were used as the catholyte and anolyte, respectively, to avoid the overlap of In and K in EDX mapping of CD-In (Figure 1k-o). More detailed analysis (Figure S6) suggested other than partially being hydrolyzed on the surface, some In species 'permeated' significantly deeper into the carbon fiber layer, likely due to the electromigration of In^{3+} cations under cathodic potential prior to the complete reduction of In^{3+}. Cl^- was also found close to the In species, probably as an adsorbate. The concentrated Cl^- inside of the carbon matrix prohibited the complete hydrolysis of In^{3+} in the alkaline solution. Notably, the presence of electrolyte flooding (Figure S6d,i,n), which is typically considered detrimental to the CO_2RR, was harnessed here to facilitate precursor migration and utilize the available pore volume within the GDE carbon matrix. This strategy mirrors a well-established concept of confinement in porous zeolites, where host structures restrict particle growth and improve stability.[23−25]

High-angle annular dark-field scanning transmission electron microscopy (HAADF-STEM) image of CD-In and OD-In catalysts also revealed distinct morphological differences. OD-In exhibited pronounced particle aggregation with the grain size of >100 nm (Figure 2a), consistent with the sintering behavior of oxide-derived metal grains under CO_2RR

conditions.[29] In contrast, CD-In consisted of well-dispersed In nanoparticles encapsulated in the carbon matrix, most of which were <15 nm in size, though a small portion of large particles (up to 50 nm) was also observed (Figure 2b). The larger particles were likely formed on the surface of GDE without the confinement of carbon matrix. XRD patterns of CD-In and OD-In showed peaks corresponding to carbon paper and metallic In (Figure 2c), while CD-In exhibited broader and less-intensive peaks for metallic In, indicative of smaller and less-crystalline particles. X-ray photoelectron spectroscopy (XPS) revealed the coexistence of metallic In and In(III) species in both samples (Figure 2d), likely resulting from air-induced surface oxidation. HAADF-STEM images with atomic resolution exhibited the existence of an amorphous (hydr)oxide shell with a thickness of ∼ 3 nm, regardless of the sizes of the single particles (Figures 2e, S7a, and S8a).

Considering the sufficient crystallinity for direct lattice analysis (Figure 2e), a fast Fourier transform (FFT) analysis, followed by inverse FFT (IFFT), was applied to selected regions of HAADF-STEM images (Figure 2e-i). Measured lattice spacings ranged from 2.609 Å to 2.713 Å (Figures S7b-e, S8b-e), all closely matching the (101) plane of metallic In (2.715 Å). For CD-In, particles smaller than 15 nm exhibited a consistent compressive strain of 2−4% (Figures 2e-i and S7), whereas larger particles in both CD-In or OD-In showed negligible deviation (<0.5%) (Figures S8 and S9). This strain effect observed on smaller particles is consistent with previous observations in confined nanoscale systems.[9,30] The crystallinity of large particles, despite their low proportion, accounted for the negligible peak shift in the XRD results (Figure 2c).
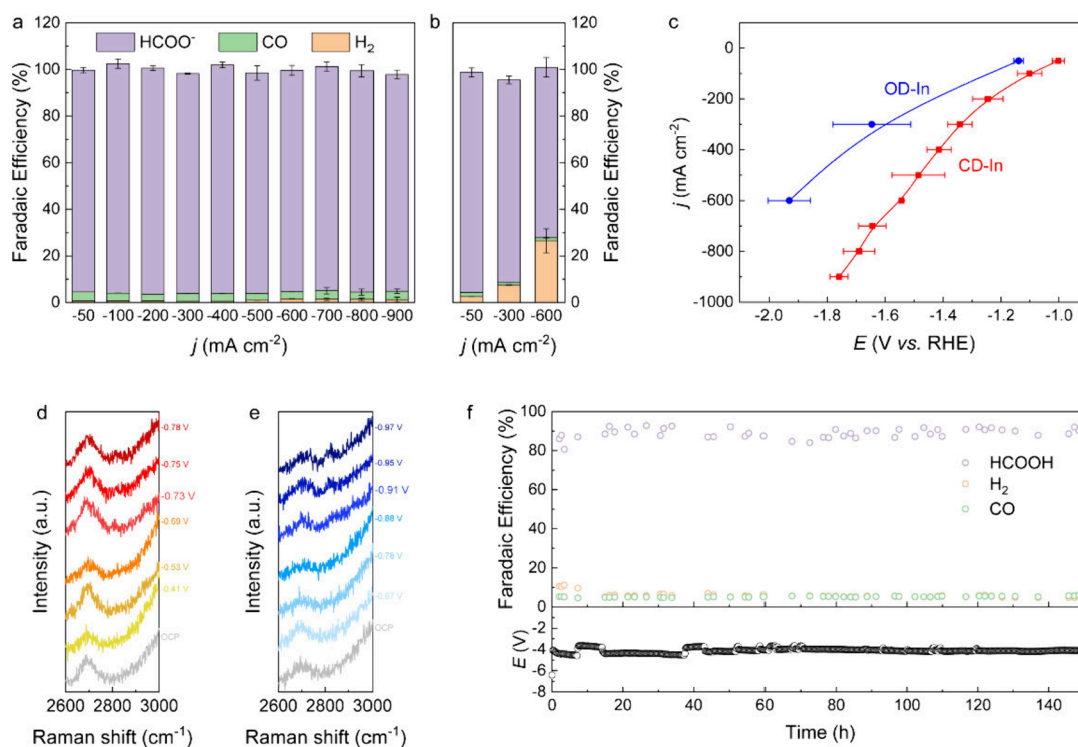
Figure 3. CO_2RR performances of CD-In and OD-In. **a)** FEs of different CO_2RR products over CD-In in 0.5 M $KHCO_3$. **b)** FEs of different CO_2RR products over OD-In in 0.5 M $KHCO_3$. **c)** j-E curves over CD-In and OD-In in 0.5 M $KHCO_3$. **d)** In situ Raman spectra over CD-In at different potentials in 0.5 M $KHCO_3$. **e)** In situ Raman spectra over OD-In at different potentials in 0.5 M $KHCO_3$. All potentials in **d** and **e** refer to potentials vs RHE. The peak located at ~ 2690 cm^{-1} was ascribed to the double resonance of D-band in graphite, while the peak located at ~ 2830 cm^{-1} was ascribed to H–C vibration of $HCOO^*$. **f)** Continuous production of pure HCOOH solution over CD-In in a solid-state electrolyte reactor. Current, 200 mA. Cathode area, 2×2 cm^2. Anolyte, 0.05 M H_2SO_4.

Apart from the oxide-shell structure, we also observed the complete oxidation of a single small particle to an amorphous (hydr)oxide (Figure S10). The X-ray absorption fine structure (XAFS) of CD-In (Figure S11) indicates the coexistence of metallic In and (hydr)oxide, which corresponded well with XPS patterns (Figure 2d) and atomic-resolution HAADF-STEM images (Figures 2e, S7a, S8a, and S10).

Leveraging the unique spatial distribution of In particles in CD-In, we evaluated its CO_2RR performance to verify our hypothesis that deeper catalyst infiltration would mitigate performance degeneration induced by the flooding issue. In a typical flow cell, CD-In exhibited a high FE for formate of >93% across a wide current density range (from −50 to −900 mA cm^{-2}), while the FE for competing HER was severely suppressed to less than 2% (Figure 3a). In contrast, OD-In prepared via a conventional spray-coating method exhibited an increase in HER FE with increasing current density (Figure 3b). The total current density over CD-In was also larger than that over OD-In at a similar applied potential (Figure 3c). Notably, dominant production of formate with a low FE for HER at a low current density of 50 mA cm^{-2} was observed both over CD-In and OD-In. The performance degeneration over OD-In could be ascribed to the flooding issue. This could be supported by the contact angle measurement result. CD-In and OD-In were both less hydrophobic on the surface compared to their precursors (Figure S4). Specifically, the contact angle on the CD-In-loaded GDL decreased with time but eventually was stabilized (Figure S4b-d), while the water droplet on the OD-In-loaded GDL was completely absorbed (Figure S4f-h). It is worth noting that contact-angle measure-

ments mainly reflect surface wetting behavior related to exposed carbon, while under the water-rich electrolysis environment, flooding already happened during the preparation phase (Figure S6d,i,n). The possible promotional influence of residual Cl^-, which has been reported to boost CO_2RR activity,[31,32] was also excluded by similar product distribution over a nitrate-derived In (ND-In) and CD-In in KCl solution (Figures S12 and S13).

Attempts to determine the intrinsic activity via electrochemical surface area (ECSA) normalization were hindered by the absence of a reliable underpotential deposition protocol for In. Quantification of electric double-layer capacitances (C_{dl}) by cyclic voltammetry was another method used for the estimation of ECSA, while one should be especially cautious about the assignment of C_{dl} to the ECSA of a carbon paper GDL. Although these two catalysts exhibited a $\sim$ 7-fold difference in C_{dl} (Figure S14), which seemed to correspond well with the different dispersion patterns evidenced by HAADF-STEM images (Figure 2a,b), we ascribed the origin of C_{dl} mainly to the exposed carbon black of GDL (Figure 2c), because C_{dl} of CD-In-loaded GDE slightly increased a little when only 10% of the original amount was loaded (Figure S15). Intriguingly, even with the low loading amount, CD-In still exhibited a similar product distribution and j-E curve (Figure S16), suggesting only a limited amount of particles participated in the reaction.

Notably, low FE for HER at −50 mA cm^{-2} for both CD-In and OD-In corresponded well with the statement from Bagger et al. that inhibition of HER ought to be feasible over formate-selective metals.[17] However, we observed that even at this low
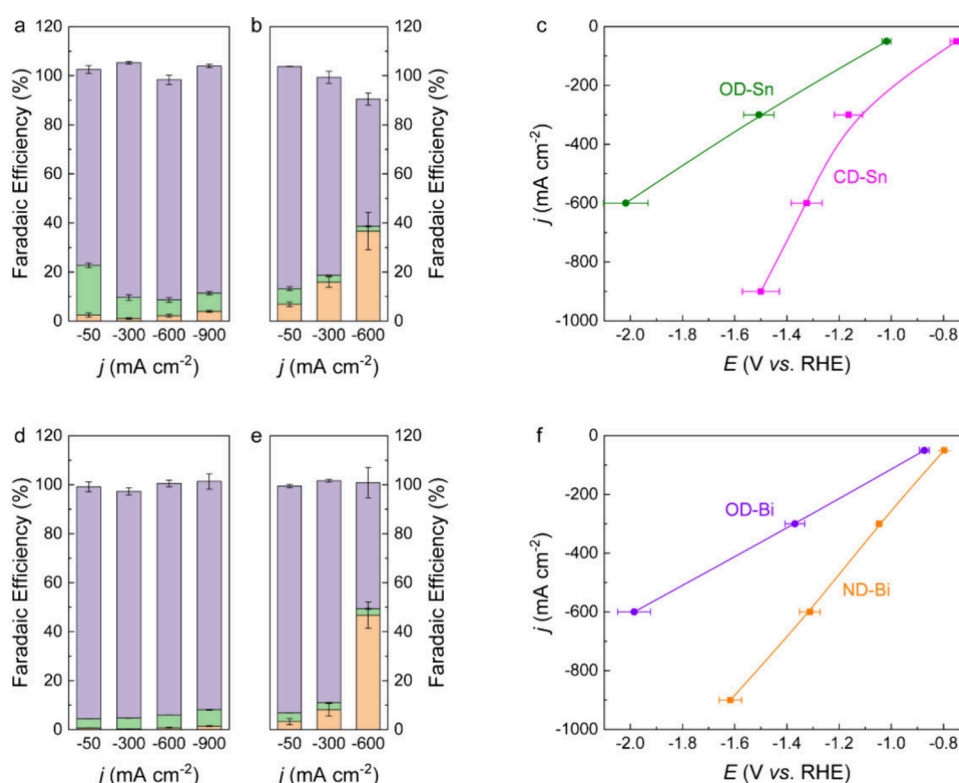
Figure 4. Universality of the soluble salt-inducing fabrication method. **a**) FEs for different CO_2RR products over CD-Sn. **b**) FEs for different CO_2RR products over OD-Sn. **c**) j-E curves over CD-Sn and OD-Sn. **d**) FEs for different CO_2RR products over ND-Bi. **e**) FEs for different CO_2RR products over OD-Bi. **f**) j-E curves over ND-Bi and OD-Bi. All experiments were conducted in 0.5 M $KHCO_3$. The colors in a) represent the same products as those in Figure 3a. Purple, $HCOO^-$. Green, CO.

current density where flooding is negligible CD-In exhibited lower overpotentials than did OD-In. Analysis on absolute intrinsic activity was not possible due to the loading-insensitivity of this system and lack of ECSA-normalized j-E curves. We managed to obtain the kinetic difference *via in situ* Raman spectroscopy (Figure 3d,e). A major peak at ∼ 2690 cm^{-1}, which we assigned to the double resonance of D-band in graphite, was observed for both samples at all applied potentials. It was less pronounced in the spectra of OD-In because the carbon was covered by the spray-coated catalyst. Beside this peak, another peak at ∼ 2830 cm^{-1}, which we assigned to C−H vibrations in the HCOO* intermediate, emerged. HCOO* formed first at −0.73 V vs reversible hydrogen electrode (RHE) over CD-In and −0.91 V vs RHE over OD-In. Tafel analysis corroborated these findings. CD-In exhibited a Tafel slope of 124.7 mV dec^{-1}, close to the theoretical value of 119 mV dec^{-1}, indicating that the rate-determining step (RDS) is the initial electron transfer to CO_2 (Figure S17a). In contrast, OD-In showed a much higher Tafel slope of 201.0 mV dec^{-1}, consistent with sluggish kinetics likely aggravated by mass transport limitations. Faster kinetics proved by Tafel slope and *in situ* Raman trend aligned well with the j-E curves (Figure 3c). Notably, all cathodic potentials applied in the above experiments were set at <−0.4 V vs RHE, well-below the reduction potential of In^{3+} reduction, suggesting that metallic In was maintained throughout the CO_2RR process and acted as the catalytically active phase, supported by previous indirect evidence,[15] though withdrawal of cathodic potential inevitably led to partial oxidation. We also hypothesize that the enhanced kinetics of CD-In might be from the unexpected compressive strain (2−4%) observed in

sub-15 nm In particles (Figures 2e-i and S7). DFT calculations were performed over pristine In and In under 3% compressive strain as model surfaces for OD-In and CD-In, respectively. The reaction energy of the key intermediate HCOO*, as evidenced by our *in situ* Raman spectra (Figure 3d,e), changes from 0.668 eV over pristine In to 0.552 eV over In with a compressive strain of 3% (Figure S17b). The RDS in the reaction profile is consistent with the results derived from the Tafel slope over CD-In. The reaction energies of COOH* and H*, which would evolve further into the gaseous products CO and H_2, respectively, are higher than that of HCOO*, regardless of the introduction of compressive strain (Figure S17c,d). These results are also consistent with the dominant production of formate at −50 mA cm^{-2}, where flooding would not drastically influence the product distribution. We also observed that the compressive strain would slightly enhance the formation of CO and inhibit HER, though this subtle inhibition of HER would not be the determining factor of completely different selectivity trends over CD-In and OD-In.

We further evaluated the long-term stability of CD-In under industrially relevant conditions. In a standard flow cell operating at a constant current density of 200 mA cm^{-2}, CD-In maintained stable performance for 55 hours (Figure S18). There still remains a fundamental limitation of aqueous catholyte-based flow cells: formate is produced in solution (*e.g.*, in $KHCO_3$ or KCl), necessitating additional downstream separation and incurring energy penalties. To overcome these issues, we employed a solid-state electrolyte (SSE) reactor system, enabling the direct collection of pure HCOOH solution with the additional benefit of facilitating *in situ* regeneration of dissolved CO_2.[12,33−35] In the SSE reactor, CD-In-

In remained selective for HCOOH as the major product with an FE above 87% across current density ranging from −50 to −250 mA cm^{-2}, but the FE for HCOOH decreased to 58% at −300 mA cm^{-2} (Figure S19). Higher FE for HER in SSE reactor was caused by the insufficient K$^+$ cation, since only a limited amount of K$^+$ residue, which remained after the pretreatment of membrane in KOH, functioned as the stabilizer for CO$_2$RR intermediate.[20] We achieved continuous and stable production of pure HCOOH at 200 mA with a FE for HCOOH of >80% for 150 hours (Figure 3f). It is also feasible to operate the SSE reactor with only CO$_2$ and pure water as inputs, while a higher cell voltage is required (Figure S20).

To evaluate the universality of our soluble-salt infiltration approach, a different commercial GDL (28BC) with different structures was also tested, and similar In distribution patterns and catalytic selectivities were observed (Figures S21 and S22). We further applied this synthesis method to other nontoxic formate-selective metals and studied their CO$_2$RR performances. Chloride-derived Sn (CD-Sn), synthesized analogously to CD-In, exhibited low FE for HER of <4% across a wide current density range (−50 to −900 mA cm^{-2}) despite a modest increase in CO production (Figure 4a). Similar to the case of OD-In, HER could not be effectively suppressed over the control sample (oxide-derived Sn and OD-Sn) (Figure 4b,c). Moreover, nitrate-derived Bi (ND-Bi) outperformed oxide-derived Bi (OD-Bi) in both the selectivity and current density (Figure 4d-f). These results collectively confirm the universality of our synthesis strategy of using soluble salt as the precursors to construct HER-resistant and high-performance GDEs. Moving forward, this platform could also be further expanded through alloying, molecular modification, or tandem catalytic design to enable broader applications in CO$_2$ electroreduction or even other electrochemical reactions involving gaseous components.

In summary, we developed a simple yet effective soluble salt-inducing fabrication strategy to encapsulate formate-selective metal catalysts within the carbon matrix of commercial carbon paper GDLs. Unlike conventional GDEs, where catalysts are deposited onto the upper surface of an electrode, this method enables deeper catalyst infiltration along the through-plane direction of the GDL. This vertically integrated architecture significantly mitigated the performance degeneration caused by flooding, preserved CO$_2$ accessibility, and thus sustained high formate selectivity. CD-In, as the model catalyst, exhibited suppressed FE for HER of <2% across a broad current density range from −50 to −900 mA cm^{-2}. A compressive strain of 2−4% was also observed in small particles confined in the carbon matrix of GDE, which was totally unexpected before the experiment, although the compressive strain additionally boosted the kinetics of formate production. Furthermore, we demonstrated the universality of this fabrication strategy across other nontoxic formate-selective metals, including Sn and Bi. This work offers a generalizable platform for designing robust, flooding-resistant GDEs for high-performance CO$_2$ electroreduction and exhibits promising potential to some other electrochemical reactions with gas involved.

◼ ASSOCIATED CONTENT

Data Availability Statement

The data associated with this article are available in the manuscript and Supporting Information.

Ⓢ Supporting Information

The Supporting Information is available free of charge at https://pubs.acs.org/doi/10.1021/acsmaterialslett.5c01489.

Experimental details, including synthesis method, electrochemical performances, characterization, and DFT calculation (PDF)

◼ AUTHOR INFORMATION

Corresponding Author

Tingting Zheng — *School of Materials and Energy, University of Electronic Science and Technology of China, Chengdu 611731, P. R. China*; Email: ttzheng@uestc.edu.cn

Authors

Chuanhao Wang — *School of Materials and Energy, University of Electronic Science and Technology of China, Chengdu 611731, P. R. China; Hefei National Research Center for Physical Sciences at the Microscale, Key Laboratory of Strongly-Coupled Quantum Matter Physics of Chinese Academy of Sciences, Key Laboratory of Surface and Interface Chemistry and Energy Catalysis of Anhui Higher Education Institutes, Department of Chemical Physics, University of Science and Technology of China, Hefei 230026, P. R. China; Max-Planck-Institut für Kohlenforschung, Mülheim an der Ruhr 45470, Germany;* ⓘ orcid.org/0000-0003-0134-5935

Yizhou Dai — *School of Materials and Energy, University of Electronic Science and Technology of China, Chengdu 611731, P. R. China; Hefei National Research Center for Physical Sciences at the Microscale, Key Laboratory of Strongly-Coupled Quantum Matter Physics of Chinese Academy of Sciences, Key Laboratory of Surface and Interface Chemistry and Energy Catalysis of Anhui Higher Education Institutes, Department of Chemical Physics, University of Science and Technology of China, Hefei 230026, P. R. China*

Xian Zhong — *School of Materials and Energy and Institute of Fundamental and Frontier Sciences, University of Electronic Science and Technology of China, Chengdu 611731, P. R. China*

Wenrui Zhang — *School of Materials and Energy, University of Electronic Science and Technology of China, Chengdu 611731, P. R. China*

Zhaoyang Chen — *School of Materials and Energy, University of Electronic Science and Technology of China, Chengdu 611731, P. R. China;* ⓘ orcid.org/0000-0002-1547-698X

Chunxiao Liu — *School of Materials and Energy, University of Electronic Science and Technology of China, Chengdu 611731, P. R. China;* ⓘ orcid.org/0000-0002-6217-4482

Yuan Ji — *School of Materials and Energy, University of Electronic Science and Technology of China, Chengdu 611731, P. R. China*

Sunpei Hu — *Hefei National Research Center for Physical Sciences at the Microscale, Key Laboratory of Strongly-Coupled Quantum Matter Physics of Chinese Academy of Sciences, Key Laboratory of Surface and Interface Chemistry and Energy Catalysis of Anhui Higher Education Institutes, Department of Chemical Physics, University of Science and Technology of China, Hefei 230026, P. R. China*

Alexander Kostis — *Max-Planck-Institut für Kohlenforschung, Mülheim an der Ruhr 45470, Germany*

Adrian Schlüter — *Max-Planck-Institut für Kohlenforschung, Mülheim an der Ruhr 45470, Germany*

Eko Budiyanto − *Max-Planck-Institut für Kohlenforschung, Mülheim an der Ruhr 45470, Germany*

Boyan Zhang − *National Synchrotron Radiation Laboratory, University of Science and Technology of China, Hefei 230029, P. R. China*

Chih-Wen Pao − *National Synchrotron Radiation Research Center, Hsinchu 300092, Taiwan;* ⊚ orcid.org/0000-0001-7681-4391

Yizhen Chen − *Department of Chemical Engineering, University of California, Davis, California 95616, United States;* ⊚ orcid.org/0000-0002-8499-2013

Florian Baum − *Max-Planck-Institut für Kohlenforschung, Mülheim an der Ruhr 45470, Germany*

Jacob Johny − *Max Planck Institute for Chemical Energy Conversion, Mülheim an der Ruhr 45470, Germany;* ⊚ orcid.org/0000-0002-5941-6348

Xu Li − *School of Materials and Energy, University of Electronic Science and Technology of China, Chengdu 611731, P. R. China;* ⊚ orcid.org/0000-0001-7577-4957

Qiu Jiang − *School of Materials and Energy, University of Electronic Science and Technology of China, Chengdu 611731, P. R. China;* ⊚ orcid.org/0000-0002-2408-198X

Hong-Jie Peng − *Institute of Fundamental and Frontier Sciences, University of Electronic Science and Technology of China, Chengdu 611731, P. R. China*

Xinyan Liu − *Institute of Fundamental and Frontier Sciences, University of Electronic Science and Technology of China, Chengdu 611731, P. R. China;* ⊚ orcid.org/0000-0002-3629-1730

Jie Zeng − *Hefei National Research Center for Physical Sciences at the Microscale, Key Laboratory of Strongly-Coupled Quantum Matter Physics of Chinese Academy of Sciences, Key Laboratory of Surface and Interface Chemistry and Energy Catalysis of Anhui Higher Education Institutes, Department of Chemical Physics, University of Science and Technology of China, Hefei 230026, P. R. China;* ⊚ orcid.org/0000-0002-8812-0298

Chuan Xia − *School of Materials and Energy, University of Electronic Science and Technology of China, Chengdu 611731, P. R. China;* ⊚ orcid.org/0000-0003-4526-159X

Complete contact information is available at:
https://pubs.acs.org/10.1021/acsmaterialslett.5c01489

Author Contributions

◼ (C.W., Y.D., X.Z.) These authors contributed equally to this work. C.W. and Y.D. conceived the idea. T.Z. supervised the project. C.W., Y.D., and W.Z. synthesized catalysts and performed CO_2RR tests. X.Z., H.P., and X.Liu conducted DFT calculations. Z.C., C.L., Y.J., X.Li, and Q.J. helped with the stability test. S.H., E.B., B.Z., A.K., A.S., C.-W.P., Y.C., F.B., and J.J. conducted characterization and analyzed results. C.W. wrote the manuscript. Y.D., C.X., J.Z., and T.Z. revised the manuscript. All authors discussed the results and commented on the manuscript.

Notes

The authors declare the following competing financial interest(s): A China provisional patent application (ZL202211017376.4) based on the technology described in this work was filed in August 2022 by C.X., C.W., and C.L. at the University of Electronic Science and Technology of China. The other authors declare no competing interests.

◼ ACKNOWLEDGMENTS

◼ REFERENCES

(1) Bushuyev, O. S.; De Luna, P.; Dinh, C. T.; Tao, L.; Saur, G.; van de Lagemaat, J.; Kelley, S. O.; Sargent, E. H. What Should We Make with CO_2 and How Can We Make It? *Joule* **2018**, *2*, 825−832.

(2) De Luna, P.; Hahn, C.; Higgins, D.; Jaffer, S. A.; Jaramillo, T. F.; Sargent, E. H. What Would It Take for Renewably Powered Electrosynthesis to Displace Petrochemical Processes? *Science* **2019**, *364*, No. eaav3506.

(3) Chen, C.; Khosrowabadi Kotyk, J. F.; Sheehan, S. W. Progress toward Commercial Application of Electrochemical Carbon Dioxide Reduction. *Chem.* **2018**, *4*, 2571−2586.

(4) Gu, J.; Hsu, C. S.; Bai, L.; Chen, H. M.; Hu, X. Atomically Dispersed Fe(3+) Sites Catalyze Efficient CO_2 Electroreduction to CO. *Science* **2019**, *364*, 1091−1094.

(5) Zhong, M.; Tran, K.; Min, Y.; Wang, C.; Wang, Z.; Dinh, C. T.; De Luna, P.; Yu, Z.; Rasouli, A. S.; Brodersen, P.; et al. Accelerated Discovery of CO_2 Electrocatalysts Using Active Machine Learning. *Nature* **2020**, *581*, 178−183.

(6) Dinh, C. T.; Burdyny, T.; Kibria, M. G.; Seifitokaldani, A.; Gabardo, C. M.; García de Arquer, F. P.; Kiani, A.; Edwards, J. P.; De Luna, P.; Bushuyev, O. S.; et al. CO_2 Electroreduction to Ethylene via Hydroxide-Mediated Copper Catalysis at an Abrupt Interface. *Science* **2018**, *360*, 783−787.

(7) Li, F.; Thevenon, A.; Rosas-Hernández, A.; Wang, Z.; Li, Y.; Gabardo, C. M.; Ozden, A.; Dinh, C. T.; Li, J.; Wang, Y.; et al. Molecular Tuning of CO_2-to-Ethylene Conversion. *Nature* **2020**, *577*, 509−513.

(8) Wang, X.; Wang, Z.; García de Arquer, F. P.; Dinh, C. T.; Ozden, A.; Li, Y. C.; Nam, D. H.; Li, J.; Liu, Y.-S.; Wicks, J.; et al. Efficient Electrically Powered CO_2-to-ethanol via Suppression of Deoxygenation. *Nat. Energy* **2020**, *5*, 478−486.

(9) Xu, H.; Rebollar, D.; He, H.; Chong, L.; Liu, Y.; Liu, C.; Sun, C.-J.; Li, T.; Muntean, J. V.; Winans, R. E.; et al. Highly Selective Electrocatalytic CO_2 Reduction to Ethanol by Metallic Clusters Dynamically Formed from Atomically Dispersed Copper. *Nat. Energy* **2020**, *5*, 623−632.

(10) Peng, C.; Luo, G.; Zhang, J.; Chen, M.; Wang, Z.; Sham, T.-K.; Zhang, L.; Li, Y.; Zheng, G. Double Sulfur Vacancies by Lithium

Tuning Enhance CO_2 Electroreduction to n-Propanol. *Nat. Commun.* **2021**, *12*, 1580.

(11) Grigioni, I.; Sagar, L. K.; Li, Y. C.; Lee, G.; Yan, Y.; Bertens, K.; Miao, R. K.; Wang, X.; Abed, J.; Won, D. H.; et al. CO_2 Electroreduction to Formate at a Partial Current Density of 930 mA cm^{-2} with InP Colloidal Quantum Dot Derived Catalysts. *ACS Energy Lett.* **2021**, *6*, 79−84.

(12) Fan, L.; Xia, C.; Zhu, P.; Lu, Y.; Wang, H. Electrochemical CO_2 Reduction to High-Concentration Pure Formic Acid Solutions in an All-Solid-State Reactor. *Nat. Commun.* **2020**, *11*, 3633.

(13) Fan, T.; Ma, W.; Xie, M.; Liu, H.; Zhang, J.; Yang, S.; Huang, P.; Dong, Y.; Chen, Z.; Yi, X. Achieving High Current Density for Electrocatalytic Reduction of CO_2 to Formate on Bismuth-Based Catalysts. *Cell Rep. Phys. Sci.* **2021**, *2*, No. 100378.

(14) Li, L.; Ozden, A.; Guo, S.; García de Arquer, F. P.; Wang, C.; Zhang, M.; Zhang, J.; Jiang, H.; Wang, W.; Dong, H.; et al. Stable, Active CO_2 Reduction to Formate via Redox-Modulated Stabilization of Active Sites. *Nat. Commun.* **2021**, *12*, 5223.

(15) Ma, L.; Liu, N.; Mei, B.; Yang, K.; Liu, B.; Deng, K.; Zhang, Y.; Feng, H.; Liu, D.; Duan, J.; et al. In Situ-Activated Indium Nanoelectrocatalysts for Highly Active and Selective CO_2 Electro-reduction around the Thermodynamic Potential. *ACS Catal.* **2022**, *12*, 8601−8609.

(16) Hori, Y. Electrochemical CO_2 Reduction on Metal Electrodes. In *Modern Aspects of Electrochemistry*; Vayenas, C. G., White, R. E., Gamboa-Aldeco, M. E., Eds.; Springer: New York, 2008; pp 89−189.

(17) Bagger, A.; Ju, W.; Varela, A. S.; Strasser, P.; Rossmeisl, J. Electrochemical CO_2 Reduction: A Classification Problem. *Chem-PhysChem* **2017**, *18*, 3266−3273.

(18) Thorson, M. R.; Siil, K. I.; Kenis, P. J. A. Effect of Cations on the Electrochemical Conversion of CO_2 to CO. *J. Electrochem. Soc.* **2013**, *160*, F69−F74.

(19) Monteiro, M. C. O.; Dattila, F.; Hagedoorn, B.; García-Muelas, R.; López, N.; Koper, M. T. M. Absence of CO_2 Electroreduction on Copper, Gold and Silver Electrodes Without Metal Cations in Solution. *Nat. Catal.* **2021**, *4*, 654−662.

(20) Shin, S. J.; Choi, H.; Ringe, S.; Won, D. H.; Oh, H.-S.; Kim, D. H.; Lee, T.; Nam, D.-H.; Kim, H.; Choi, C. H. A Unifying Mechanism for Cation Effect Modulating C_1 and C_2 Productions from CO_2 Electroreduction. *Nat. Commun.* **2022**, *13*, 5482.

(21) Weitzner, S. E.; Akhade, S. A.; Varley, J. B.; Wood, B. C.; Otani, M.; Baker, S. E.; Duoss, E. B. Toward Engineering of Solution Microenvironments for the CO_2 Reduction Reaction: Unraveling pH and Voltage Effects from a Combined Density-functional-continuum Theory. *J. Phys. Chem. Lett.* **2020**, *11*, 4113−4118.

(22) Disch, J.; Bohn, L.; Koch, S.; Schulz, M.; Han, Y.; Tengattini, A.; Helfen, L.; Breitwieser, M.; Vierrath, S. High-resolution Neutron Imaging of Salt Precipitation and Water Transport in Zero-gap CO_2 Electrolysis. *Nat. Commun.* **2022**, *13*, 6099.

(23) Choi, M.; Wu, Z.; Iglesia, E. Mercaptosilane-assisted Synthesis of Metal Clusters Within Zeolites and Catalytic Consequences of Encapsulation. *J. Am. Chem. Soc.* **2010**, *132*, 9129−9137.

(24) Goel, S.; Zones, S. I.; Iglesia, E. Encapsulation of Metal Clusters within MFI via Interzeolite Transformations and Direct Hydro-thermal Syntheses and Catalytic Consequences of Their Confine-ment. *J. Am. Chem. Soc.* **2014**, *136*, 15280−15290.

(25) Zhu, J.; Osuga, R.; Ishikawa, R.; Shibata, N.; Ikuhara, Y.; Kondo, J. N.; Ogura, M.; Yu, J.; Wakihara, T.; Liu, Z.; et al. Ultrafast Encapsulation of Metal Nanoclusters into MFI Zeolite in the Course of its Crystallization: Catalytic Application for Propane Dehydrogen-ation. *Angew. Chem., Int. Ed.* **2020**, *59*, 19669−19674.

(26) Kong, X.; Wang, C.; Xu, Z.; Zhong, Y.; Liu, Y.; Qin, L.; Zeng, J.; Geng, Z. Enhancing CO_2 Electroreduction Selectivity toward Multicarbon Products via Tuning the Local H_2O/CO_2 Molar Ratio. *Nano Lett.* **2022**, *22*, 8000−8007.

(27) Lamaison, S.; Wakerley, D.; Kracke, F.; Moore, T.; Zhou, L.; Lee, D. U.; Wang, L.; Hubert, M. A.; Aviles Acosta, J. E.; Gregoire, J. M.; et al. Designing a Zn−Ag Catalyst Matrix and Electrolyzer System for CO_2 Conversion to CO and Beyond. *Adv. Mater.* **2022**, *34*, No. 2103963.

(28) Wang, X.; Chen, Q.; Zhou, Y.; Tan, Y.; Wang, Y.; Li, H.; Chen, Y.; Sayed, M.; Geioushy, R. A.; Allam, N. K.; et al. Gas Diffusion in Catalyst Layer of Flow Cell for CO_2 Electroreduction toward C_{2+} Products. *Nano Res.* **2024**, *17*, 1101−1106.

(29) Yang, Y.; Louisia, S.; Yu, S.; Jin, J.; Roh, I.; Chen, C.; Fonseca Guzman, M. V.; Feijóo, J.; Chen, P.-C.; Wang, H.; et al. Operando Studies Reveal Active Cu Nanograins for CO_2 Electroreduction. *Nature* **2023**, *614*, 262−269.

(30) Guvelioglu, G. H.; Ma, P.; He, X.; Forrey, R. C.; Cheng, H. First Principles Studies on the Growth of Small Cu Clusters and the Dissociative Chemisorption of H_2. *Phys. Rev. B* **2006**, *73*, No. 155436.

(31) Fu, H. Q.; Zhang, L.; Zheng, L. R.; Liu, P. F.; Zhao, H.; Yang, H. G. Enhanced CO_2 Electroreduction Performance over Cl-modified Metal Catalysts. *J. Mater. Chem. A* **2019**, *7*, 12420−12425.

(32) Li, S.; Dong, X.; Zhao, Y.; Mao, J.; Chen, W.; Chen, A.; Song, Y.; Li, G.; Jiang, Z.; Wei, W.; et al. Chloride Ion Adsorption Enables Ampere-level CO_2 Electroreduction over Silver Hollow Fiber. *Angew. Chem., Int. Ed.* **2022**, *61*, No. e202210432.

(33) Xia, C.; Zhu, P.; Jiang, Q.; Pan, Y.; Liang, W.; Stavitski, E.; Alshareef, H. N.; Wang, H. Continuous Production of Pure Liquid Fuel Solutions via Electrocatalytic CO_2 Reduction Using Solid-electrolyte Devices. *Nat. Energy* **2019**, *4*, 776−785.

(34) Zheng, T.; Liu, C.; Guo, C.; Zhang, M.; Li, X.; Jiang, Q.; Xue, W.; Li, H.; Li, A.; Pao, C.-W.; et al. Copper-catalysed Exclusive CO_2 to Pure Formic Acid Conversion via Single-atom Alloying. *Nat. Nanotechnol.* **2021**, *16*, 776−785.

(35) Kim, J. Y. T.; Zhu, P.; Chen, F.-Y.; Wu, Z.-Y.; Cullen, D. A.; Wang, H. Recovering Carbon Losses in CO_2 Electrolysis Using a Solid Electrolyte Reactor. *Nat. Catal.* **2022**, *5*, 288−299.